

ARTICLE

<https://doi.org/10.1038/s41467-019-09072-6>

OPEN

Exploring the ternary interactions in Cu-ZnO-ZrO₂ catalysts for efficient CO₂ hydrogenation to methanol

Yuhao Wang^{1,2}, Shyam Kattel³, Wengui Gao^{1,2}, Kongzhai Li^{1,4}, Ping Liu³, Jingguang G. Chen^{3,5} & Hua Wang^{1,6}

The synergistic interaction among different components in complex catalysts is one of the crucial factors in determining catalytic performance. Here we report the interactions among the three components in controlling the catalytic performance of Cu-ZnO-ZrO₂ (CZZ) catalyst for CO₂ hydrogenation to methanol. The in situ diffuse reflectance infrared Fourier transform spectroscopy (DRIFTS) measurements under the activity test pressure (3 MPa) reveal that the CO₂ hydrogenation to methanol on the CZZ catalysts follows the formate pathway. Density functional theory (DFT) calculations agree with the in situ DRIFTS measurements, showing that the ZnO-ZrO₂ interfaces are the active sites for CO₂ adsorption and conversion, while the presence of metallic Cu is also necessary to facilitate H₂ dissociation and to provide hydrogen resource. The combined experiment and DFT results reveal that tuning the interaction between ZnO and ZrO₂ can be considered as another important factor for designing high performance catalysts for methanol generation from CO₂.

¹State Key Laboratory of Complex Nonferrous Metal Resources Clean Utilization Engineering, Kunming University of Science and Technology, Kunming 650093, China. ²Faculty of Metallurgical and Energy Engineering, Kunming University of Science and Technology, Kunming 650093, China. ³Chemistry Division, Brookhaven National Laboratory, Upton, NY 11973, USA. ⁴Department of Earth and Environmental Engineering, Columbia University, New York, NY 10027, USA. ⁵Department of Chemical Engineering, Columbia University, New York, NY 10027, USA. ⁶School of Pharmacy and Chemistry, Dali University, Dali 671003, China. These authors contributed equally: Yuhao Wang, Shyam Kattel. Correspondence and requests for materials should be addressed to K.L. (email: kongzhai.li@foxmail.com) or to J.G.C. (email: jgchen@columbia.edu) or to H.W. (email: wanghua65@163.com)

Methanol is an important chemical and energy carrier. The catalytic synthesis of methanol from CO₂ (CO₂ + 3H₂ → CH₃OH + H₂O) has attracted considerable attention, because it is not only a potential way to mitigate CO₂ emission but also an alternative process for methanol synthesis in chemical industry^{1–5}. Cu/ZnO-based catalysts (e.g., Cu–ZnO–Al₂O₃ and Cu–ZnO–ZrO₂) are the most widely studied for this process due to the high activity, high product selectivity, and low cost^{2,3,6,7}. As a promising support and promoter, ZrO₂ shows weak hydrophilic character in comparison to Al₂O₃, potentially inhibiting the poisoning effect of water on the active sites during methanol synthesis^{8–10}. The presence of ZrO₂ could also enhance the copper dispersion as well as the surface basicity, which should strongly affect the CO₂ adsorption and methanol selectivity^{11,12}. As a result, the Cu–ZnO–ZrO₂ (CZZ) system has gained an increasing interest for its outstanding activity^{1,8,9,11–17}.

Despite great efforts, the reaction mechanism of CO₂ hydrogenation to methanol as well as the nature of the active sites on CZZ catalysts are still under debate and are not comprehensively understood due to the complexity of the ternary system^{2,3,7,16,18,19}. In order to simplify the issues, binary catalyst models (e.g., Cu/ZnO and Cu/ZrO₂) have been widely used to discuss the reaction mechanism. A general conclusion is that methanol synthesis over Cu-based catalysts is a structure-sensitive reaction and the synergetic effect between Cu and oxides is responsible for the enhanced activity^{3,5,10,20–27}. The Cu/ZnO synergy is proposed to create active sites for CO₂ and H₂ conversion via a combination of defective Cu nanoparticles with ZnO thin overlayer (including induced morphological changes of Cu)^{22,24,28}, junction effect at the Cu–ZnO interface (including enhanced electron transfer and increased generation of oxygen defects in the interface)^{3,5,29–31}, or formation of a specific Cu–Zn surface alloy (including migration of Zn atoms over the Cu surface and incorporation of Zn atoms into the Cu step-edge sites)^{7,19,21}. The Cu/ZrO₂ synergy is mainly attributed to the formation of Cu–ZrO₂ interfacial sites, which may promote the adsorption of CO₂^{10,26}, enhance the dissociation of H₂ and spillover of atomic hydrogen^{32,33}, bind the key reaction intermediates (*CO₂, *CO, *HCO, and *H₂CO) for further conversion²⁷, and increase the turnover frequency²⁶.

The role of ZnO–ZrO₂ interaction is an ongoing debate. Recently, it was reported that the binary ZnO–ZrO₂ oxide in the solid solution state also shows activity for CO₂ hydrogenation to methanol³⁴. The Zn-doped ZrO₂ without the presence of Cu could achieve high CO₂ conversion (10%) and methanol selectivity (86%) at high pressure (5 MPa) and high temperature (593 K). In comparison, CZZ catalysts with the presence of Cu usually could obtain high methanol yield at moderate conditions (3 MPa and 493–513 K, see the comparison in Supplementary Table 3). However, little is known about the atomic-level interaction among the three components in the Cu–ZnO–ZrO₂ complex system, in particular under in situ reaction conditions.

Here, we report a mechanistic investigation of the ternary interactions of Cu/ZnO/ZrO₂ in CO₂ adsorption and activation for methanol synthesis by comparing the three-dimensional ordered macroporous (3DOM) catalysts with different particle size of ZnO. The 3DOM catalyst shows very high activity (18.2% CO₂ conversion and 80.2% methanol selectivity obtained at 493 K and 3.0 MPa). The results from the in situ DRIFTS measurements at an activity test pressure (3 MPa) and DFT calculations indicate that the synergy among Cu, ZnO, and ZrO₂ is essential to promote the CO₂ conversion and methanol selectivity. The presence of Cu is necessary to allow the formation of active *H at the Cu–ZnO or Cu–ZrO₂ interface for the final formation of methanol, while the ZnO–ZrO₂ interface strongly enhances the activation and transformation of CO₂ by promoting the

hydrogenation of carbonate intermediate to more reactive species (e.g., formate and methoxy).

Results

Structural characterization. 3DOM catalysts with different particle sizes of ZnO were prepared. The full details for all samples are collected in the Supplementary Information (SI) including the (HR) TEM images, size distributions of ZnO and ZrO₂, XRD patterns, and specific surface areas of different samples. The average particle size of ZnO in the four 3DOM samples changes from 15 to 36 nm, and the ZrO₂ particles are much smaller (3–4 nm) for all the samples (Supplementary Fig. 1). The specific surface areas (Supplementary Table 1) for the 3DOM samples are in the range of 32–35 m²/g.

The EDS and TEM analyses (Fig. 1b–d) suggest that Cu makes up the 3DOM framework, and the ZnO particles are well dispersed on the wall of the macropores. The HRTEM images (Fig. 1e–g) show that t-ZrO₂ nanoparticles (3.5 ± 1 nm, Supplementary Fig. 1), with a fringe spacing of 0.295 nm corresponding to the (011) plane, are highly dispersed on both the ZnO particles and Cu framework. The structural diagrammatic sketch of macroporous CZZ catalysts is shown in Fig. 1h. The XRD patterns, shown in Supplementary Fig. 2, reveal that the diffraction peak positions corresponding to Cu or ZrO₂ are very similar for all the four samples. However, the differences in the peak widths of ZnO suggest changes of ZnO crystallite size in different samples, supporting the observation by TEM (see Supplementary Fig. 1).

Catalytic performance and reaction intermediates. Figure 2a shows the CO₂ conversion, MeOH selectivity/yield and TOF value of methanol formation as a function of the ZnO particle size. The detailed data on the physicochemical and catalytic properties of different samples (e.g., diameter of Cu (d_{Cu}), specific surface area of Cu (S_{Cu}) and turnover frequency (TOF) values) are presented in Supplementary Tables 1, 2. As seen in Fig. 2a, the 3DOM catalyst with the smallest ZnO particles (M-CZZ(16) sample) possesses very high CO₂ conversion (18.2%), methanol selectivity (80.2%) and methanol yield (297 g_{MeOH}·Kg_{Cata}⁻¹ h⁻¹). To our knowledge, this catalyst is the most active for CO₂ hydrogenation to methanol among the CZZ catalysts under comparable conditions (Supplementary Table 3). It should be highlighted that the catalytic activity of the catalysts strongly relies on the ZnO particles. The CO₂ conversion, methanol selectivity and the TOF value decrease with increasing ZnO particle size, suggesting that ZnO particles play a significant role in determining the catalytic performance.

Figure 2b–d show the DRIFT spectra obtained during CO₂ hydrogenation at 493 K and 3 MPa over the M-CZZ(16) and M-CZZ(36) catalysts. For the M-CZZ(16) sample (Fig. 2b), strong bands at 1589, 1386, and 1362 cm⁻¹ are observed, which are assigned to the $\nu_{as}(\text{OCO})$, $\delta(\text{CH})$, and $\nu_s(\text{OCO})$ modes of formate species²⁷, respectively. After the reaction proceeding for 10 min, vibrational bands at 1056, 1031, and 1005 cm⁻¹ corresponding to the C–O stretch of methanol are observed, and bands at 2975, 2943, 2920, 2871, 2840, and 2818 cm⁻¹, attributed to the C–H stretch of methanol, are also detected³⁵, indicating the formation of methanol. The comparison of the in situ DRIFT spectra of methanol and methoxy is shown in the SI (see the Supplementary Fig. 4 and the related discussion). On the other hand, peaks at 2175 and 2115 cm⁻¹, which are characteristic of gaseous CO, are also observed, indicating the occurrence of the reverse water-gas shift (RWGS) reaction. The weak and oscillating bands located in the range of 1400–1800 cm⁻¹ are attributed to water vapor, which originates from the RWGS and methanol synthesis reactions³⁶.

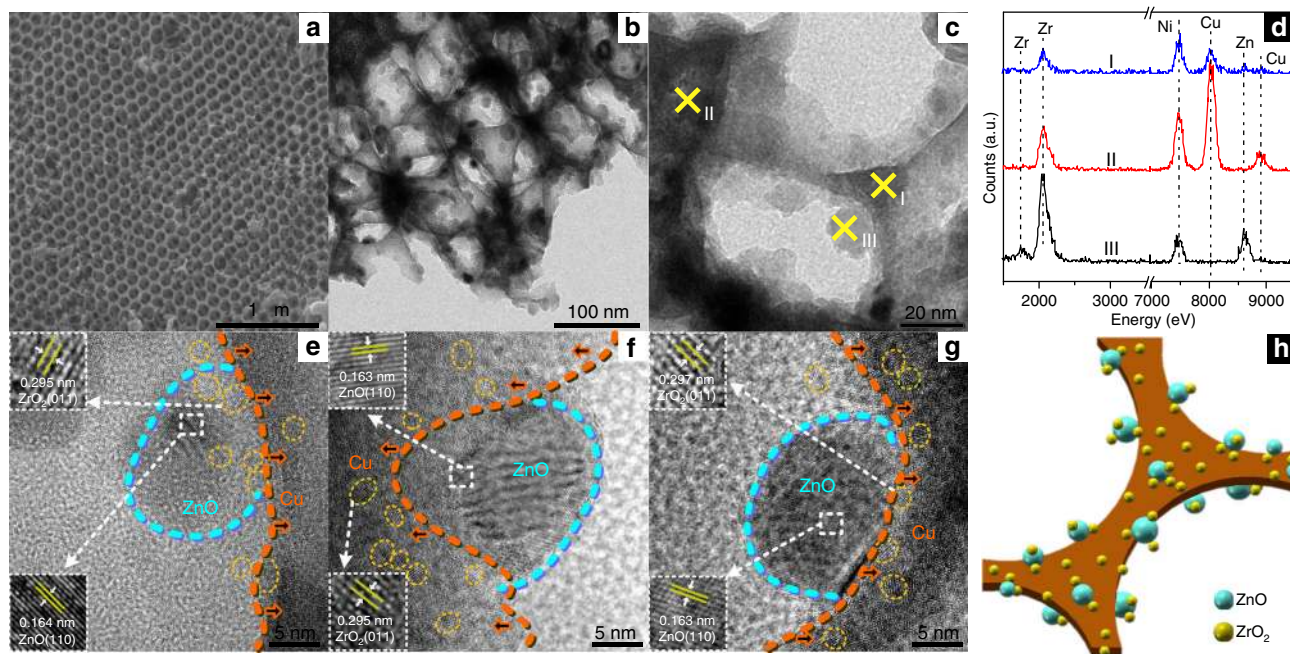


Fig. 1 Morphological and compositive characterizations of a 3DOM CZZ catalyst (M-CZZ(16)). **a** SEM image, indicating an average pore size of 120 nm. **b, c** TEM images of the M-CZZ(16) sample, which shows the smallest ZnO particle size (15.8 nm) in the 3DOM catalyst series. **d** EDS of different points in **c**. **e-g** HRTEM images of M-CZZ(16). **h** Structural diagrammatic sketch of the macroporous catalysts

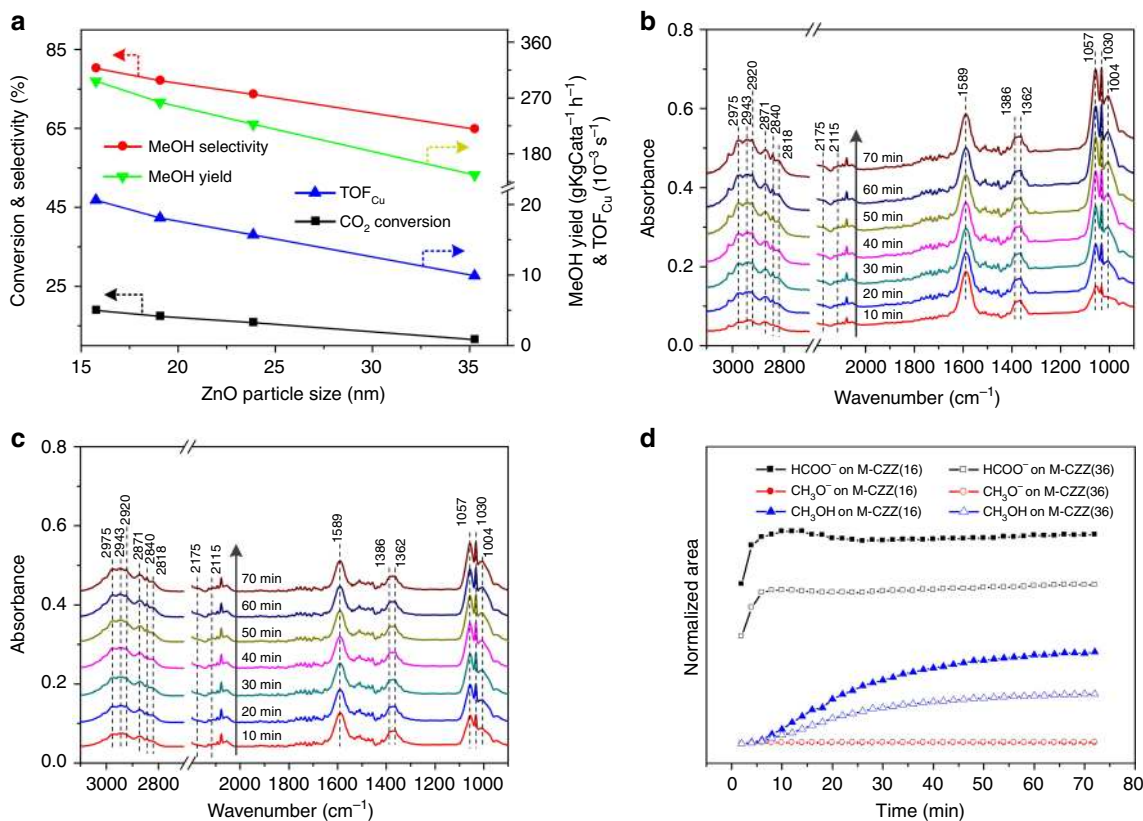


Fig. 2 Catalytic performance and in situ DRIFT spectra of the CO₂ + H₂ reaction over different catalysts. **a** CO₂ conversion, MeOH selectivity, MeOH yield and TOF values as a function of the ZnO particle sizes in different catalysts. **b** Evolution of the IR spectra over the M-CZZ(16) sample with time. **c** DRIFT spectra over the M-CZZ(36) sample. **d** Peak areas of generated intermediate species and methanol during the experiments: areas normalized to the values observed at the end of the transient. Reaction conditions for catalytic test: WHSV = 3 h⁻¹, T = 493 K, CO₂:H₂ = 1:3, P = 3.0 MPa; Reaction conditions for TOF calculation: WHSV = 10 h⁻¹, T = 493 K, CO₂:H₂ = 1:3, P = 3.0 MPa; Reaction conditions for in situ DRIFT spectra: gas flow rate = 40 mL/min, T = 493 K, CO₂:H₂ = 1:3, P = 3.0 MPa. Formate species (2870, 1589, 1386, and 1362 cm⁻¹) and methanol (2975, 2943, 2920, 2871, 2840, and 2818 cm⁻¹) can be observed over the two samples, especially for the M-CZZ(16) catalyst

In Fig. 2c, the corresponding bands observed over M-CZZ(16) are also detected over the M-CZZ(36) sample, but the band intensities of formate species and methanol are much weaker. This indicates that the particle size of ZnO affects the formation and evolution of intermediate species, and smaller ZnO particles enhance the formation of formate and methanol.

The temporal evolution of the principal surface species (formate, methoxy, and methanol) on both samples during the CO₂ hydrogenation process are presented in Fig. 2d. The concentration of formate increases sharply at the beginning of the reaction, which is followed by a slight increase of methanol. This indicates that the formation of formate is very fast, while the generation of methanol needs an induction period. It should be highlighted that the methoxy species, which is a common intermediate observed by in situ IR under atmospheric or lower pressures^{27,34}, is almost absent over the present samples. To identify the relationship between formate and methoxy species, the in situ DRIFTS experiment under atmospheric pressure is also performed, and the results are shown in Supplementary Fig. 5.

After the catalysts were pre-treated in flowing pure CO₂ for 10 min at 493 K, transient response spectra were recorded with switching H₂ into the reactor chamber. As shown in Supplementary Figs. 5a and b, before the switching, only peaks at ca. 1522 and 1352 cm⁻¹ related to monodentate (m-CO₃²⁻) and bidentate (b-CO₃²⁻) carbonate species, as well as the peak at 1075 cm⁻¹ assigned to carbonate ion (CO₃²⁻), are detected^{37,38}. The bands for formate species located at ca. 2972, 2878, 1588, 1384, and 1367 cm⁻¹ appear as soon as H₂ is introduced, while the peaks attributed to carbonate species almost disappear. This indicates that the carbonate could rapidly reacts with H to form formate.

It is also observed that the bands of formate slightly decrease in intensity with time, and the C–H (2930 and 2821 cm⁻¹) and C–O (1145 and 1045 cm⁻¹) stretching features²⁷ attributed to the methoxy gradually increase in intensity. This suggests that methoxy should originate from the hydrogenation of formate species. After the reaction proceeds for 10 min, the bands related to water vapor (see the insert in Supplementary Figs. 5a and 5b) located in the range of 1400–1800 cm⁻¹ are observed³⁶, which is likely produced from the hydrogenation of formate. The evolution of surface species over catalysts during the onset of switching feed gas from CO₂ to H₂ after CO₂ adsorption is presented in Supplementary Fig. 4c. It is clear that the intensity of methoxy slightly increases with the decrease in the formate intensity, evidencing the conversion of formate to methoxy. It is also noted that no CO intermediate is detected during the DRIFTS experiment under atmospheric pressure (see Supplementary Fig. 5), which is inconsistent with the formation of CO in the CO₂ hydrogenation at 3.0 MPa (see Fig. 2). This reveals that the reaction pressure also affects the production of CO from CO₂.

To eliminate the effect of 3DOM structure on the adsorption and catalytic activity, a series of conventional samples with various particle size of ZnO but comparable Cu and ZrO₂ particle sizes were also prepared (which were labeled as nonporous samples, N-CZZ). All the characterization, catalytic tests and in situ DRIFT experiments, which were performed on the 3DOM samples, were also performed on the N-CZZ catalysts. The results are shown in Supplementary Figs. 6–9 and Supplementary Tables 1 and 2. It is found that the catalytic performance and the evolution of the intermediate species during the reaction also strongly rely on the particle size of ZnO. This suggests that the size effect of ZnO is a common phenomenon for the CZZ catalyst system.

Comparison on Cu–ZnO, Cu–ZrO₂, and ZnO–ZrO₂ interactions. As observed above, the ZnO particle size strongly affects the CO₂ adsorption, the formation of intermediate species and

the methanol generation over the CZZ catalysts. On the other hand, the microstructures of Cu particles (e.g., Cu dispersion, Cu specific surface area and Cu particle size) in all the samples are similar (see Supplementary Table 1), and there is no direct correlation between the TOF values or methanol yields and the Cu surface area or Cu dispersion (see Supplementary Table 2). This suggests that the determining factor for the catalytic performance should be more complicated than the independent Cu related species. The size effect of ZnO may be related to the ZnO–ZrO₂ interaction. To identify the roles of Cu–ZnO, Cu–ZrO₂, and ZnO–ZrO₂ interactions in CO₂ adsorption and conversion, in situ DRIFT experiments were performed on all the three binary samples with switching the feed gas from CO₂ to H₂. The crystallite sizes of different phases in the three samples are controlled in a comparable range to ensure the comparability (see Supplementary Fig. 10).

Figure 3a shows the transient evolution of the principal surface species over the Cu–ZnO sample. In the CO₂ atmosphere, the carbonate species (1522, 1329, and 1045 cm⁻¹) are observed. After switching gas to H₂, the carbonate species disappear and very weak formate bands (1588, 1387, and 1365 cm⁻¹) are detected. Similar phenomena are also observed on the Cu–ZrO₂ sample (Fig. 3b). This indicates that the conversion of carbonate species to formate species is very difficult on these two binary samples. In contrast, abundant formate species (2972, 2878, 1593, 1386, and 1362 cm⁻¹) are formed after switching CO₂ to H₂ on the ZnO–ZrO₂ sample (Fig. 3c), concurrent with the decrease of carbonate species (Fig. 3d). The in situ DRIFT experiments at atmosphere or 3 MPa in the CO₂/H₂ mixture also reveal that only the ZnO–ZrO₂ system shows relatively high intensity of formate bands among the three samples (Supplementary Figs. 11, 12). But it should be noted that no methanol is detected over the ZnO–ZrO₂ sample at the activity test condition without the presence of Cu (see Supplementary Fig. 12c). These phenomena suggest that the ZnO–ZrO₂ interface should be the active sites for CO₂ adsorption to carbonate species and its subsequent conversion to formate and the Cu species may contribute to the further hydrogenation process.

To further study the effect of the ZnO–ZrO₂ interaction on the CO₂ adsorption and formate formation, a series of ZnO–ZrO₂ samples with different particle sizes of ZnO and similar particle sizes (average sizes of 3–4 nm) of ZrO₂ were prepared. The typical TEM images of different samples are shown in Supplementary Fig. 14. The average particle sizes for the three samples (ZnO(15)–ZrO₂, ZnO(21)–ZrO₂, and ZnO(42)–ZrO₂) are 15.1, 21.4, and 42.2 nm, respectively.

Figure 4a–c represent the in situ DRIFT spectra over the samples when switching the feed gas from CO₂ to H₂. As shown in Fig. 4a, only carbonate species (1540, 1408, and 1084 cm⁻¹) are observed over the ZnO(15)–ZrO₂ sample in CO₂. After switching the feed gas from CO₂ to H₂, the formate bands (2972, 2878, 1590, 1386, and 1363 cm⁻¹) appear immediately with the decrease of carbonate, indicating the hydrogenation of carbonate to formate. Figures 4b, c show similar trend over the ZnO(21)–ZrO₂ and ZnO(42)–ZrO₂ samples. It is notable that the formation of carbonate and its further conversion to formate is inversely proportion to the ZnO particle size. Smaller ZnO particles promote the adsorption of CO₂ and its further conversion to formate, which may be attributed to the more abundance of the ZnO–ZrO₂ interface.

In order to further understand the interaction between ZnO and ZrO₂, we have performed CO₂-TPD experiments over the ZnO(15)–ZrO₂ sample, pure ZnO particles with different average sizes (11, 19, and 37 nm) and pure ZrO₂ with an average particle size of 10 nm. As shown in Fig. 4d, the CO₂ adsorption capacity slightly decreases with increasing ZnO particle size.

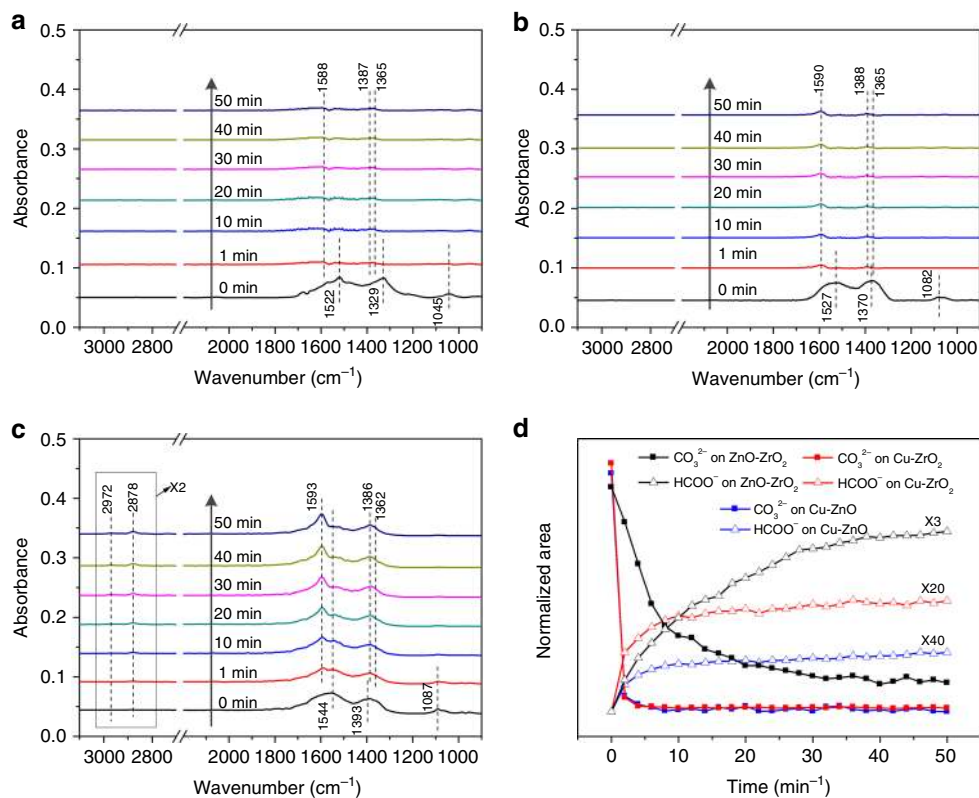


Fig. 3 Comparison on the surface species on Cu-ZnO, Cu-ZrO₂, and ZnO-ZrO₂ systems in the designed conditions. **a–c** In situ DRIFT spectra over **a** Cu-ZnO, **b** Cu-ZrO₂, and **c** ZnO-ZrO₂ materials at 493 K after switching feed gas from CO₂ (CO₂ has been loaded into the chamber for 10 min) to H₂ with a flow rate of 40 mL/min under atmosphere pressure. **d** Peak areas of generated intermediate species during the experiments: areas normalized to the values observed at the end of the transient. Only the ZnO-ZrO₂ sample shows obvious formation of formate species (2972, 2878, 1593, 1386, and 1362 cm⁻¹) from carbonate species when the feed gas was switched from CO₂ to H₂

In comparison, the ZnO(15)-ZrO₂ sample shows much higher CO₂ adsorption peak at low temperatures (373–473 K) than the pure ZrO₂ or ZnO regardless of the particle size, indicating that the interaction between ZnO and ZrO₂ strongly improves the CO₂ adsorption capacity.

Oxygen vacancy also plays a very important role in the hydrogenation of CO or CO₂ to methanol, which can adsorb and activate reactive gases and stabilize the reaction intermediates, elevating the catalytic activity^{21,22,24}. Kurtz et al.³⁹ found that the oxygen vacancy in the ZnO/Al₂O₃ catalyst is the active site for hydrogenation of CO to methanol. For Cu-ZnO catalysts in CO₂ hydrogenation, it is proposed that the activity is correlated to the number of oxygen defects between Cu and ZnO particles²². In the case of Cu-ZrO₂ catalysts, the oxygen vacancies created by the evolution of ZrO₂ phase also strongly affect the methanol formation. According to the literatures^{40,41}, catalysts with monoclinic ZrO₂ (m-ZrO₂) are nearly an order of magnitude more active for methanol synthesis from CO₂ than catalysts with the same Cu surface density deposited on tetragonal ZrO₂ (t-ZrO₂) due to the relatively higher concentration of oxygen vacancies. The formation of oxygen vacancies resulting from the ZnO-ZrO₂ interaction is evidenced by comparing the XPS spectra of ZnO/ZrO₂ sample with that of pure ZnO or ZrO₂ (see Supplementary Fig. 17 and the related discussions). Such oxygen vacancies can be the active sites for CO₂ adsorption.

For CO₂ hydrogenation to methanol over Cu-based catalysts, formate pathway (featured by formate as the main intermediate) and CO-Hydro pathway (featured by the CO intermediate produced via RWGS) are considered as two major reaction mechanisms⁵. The formate pathway is defined by the following

two conditions: (1) formate can be quickly generated and not easily decomposed into CO and (2) formate should not be excessively stable and can be hydrogenated to methoxy. In the present work, it can be seen from Supplementary Figs. 5 and 9 that the carbonate is rapidly converted to formate in the presence of H₂ and no CO is detected in this process. Meanwhile, the DRIFTS intensity of *CH₃O increases along with the decrease of the *HCOO signal. It is also found that the samples with more detectable formate in the DRIFTS experiments show higher activity for methanol formation (see Fig. 2), indicating that the formate (instead of being a spectator) should be an important intermediate for the formation of methanol. By contrast, no direct correlation is found between the formation of CO and the yield of methanol. These phenomena suggest that the CO₂ hydrogenation over the present CZZ catalysts follows the formate pathway.

Density functional theory studies. DFT calculations were performed to understand the catalytic behavior of the ZrO₂/ZnO interface during CO₂ conversion to CH₃OH. Herein, the ZrO₂/ZnO interface is modeled by depositing a small ZrO₂ cluster on the ZnO(11 $\bar{2}$ 0) surface (for details see computational method section in the SI). The surface O atoms in our model were saturated with H atoms to account for the possible H spillover from Cu to oxide nanoparticles due to facile H₂ dissociation on Cu, as predicted by DFT calculations and observed in our experiments.

Figure 5a and Supplementary Fig. 25 show the reaction intermediates that are involved in CO₂ hydrogenation, and the structure of the intermediates with different views can be found in Supplementary Fig. 26. The binding energy (−2.32 eV) for CO₂

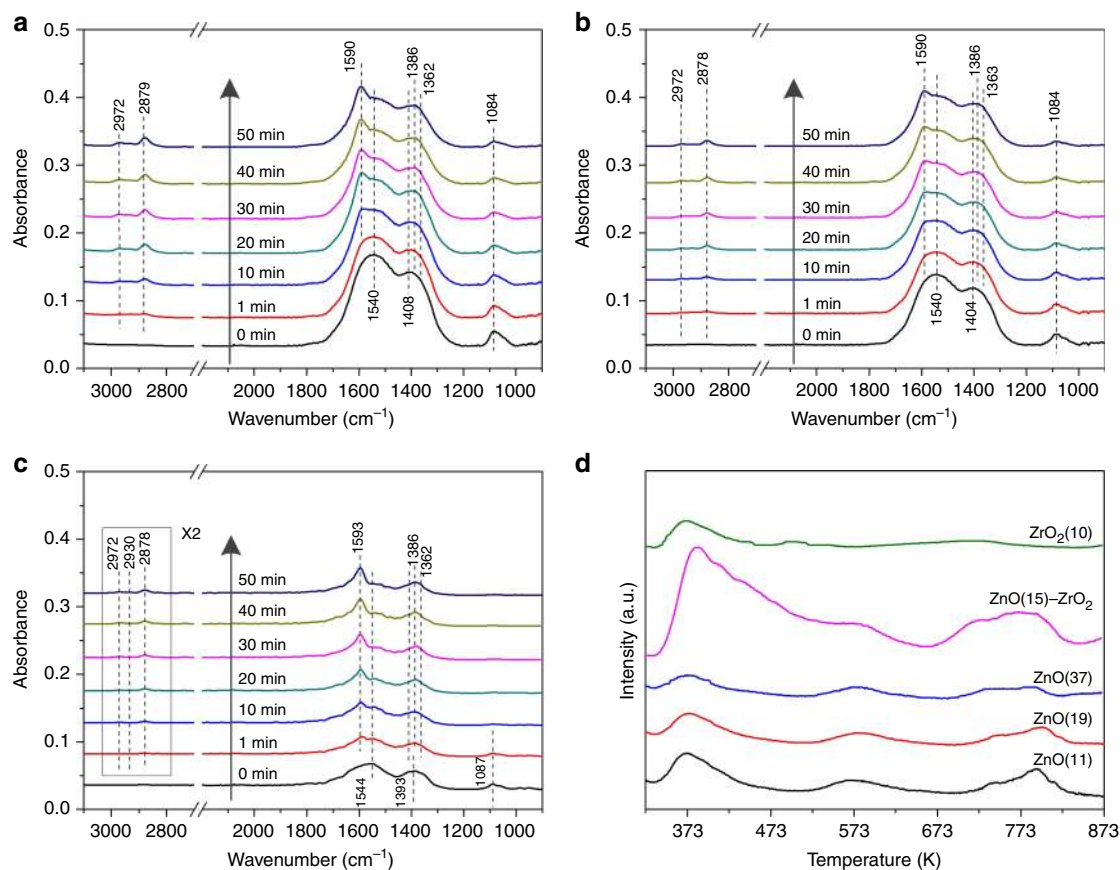


Fig. 4 Characterization of the surface species on the ZnO–ZrO₂ samples with different particles size of ZnO. In situ DRIFT spectra of **a** ZnO(15)–ZrO₂, **b** ZnO(21)–ZrO₂, and **c** ZnO(42)–ZrO₂ at 493 K after switching the feed gas from CO₂ to H₂ with a flow rate of 40 mL/min under atmosphere pressure. **d** CO₂-TPD patterns of ZnO(15)–ZrO₂, pure ZnO with different particle sizes and pure ZrO₂ with an average particle size of 10 nm

adsorption on ZrO₂–ZnO(11 $\bar{2}$ 0) is much stronger than that for ZnO–Cu(111) (–0.13 eV), ZrO₂–Cu(111) (–1.18 eV), ZrO₂ cluster on ZnO(11 $\bar{2}$ 0) (–1.95 eV), and ZnO(11 $\bar{2}$ 0) (–1.94 eV), indicating that the activation and transformation of CO₂ prefer to occur at the ZrO₂/ZnO interface.

Previously, the role of ZnO for CO₂ hydrogenation has been debated and previous studies have suggested that ZnO acts as an active phase for CO₂/CO hydrogenation to CH₃OH^{42,43}. The CO₂ → CH₃OH conversion on ZnO(11 $\bar{2}$ 0) is further investigated using DFT. The results suggest that the initial hydrogenation of CO₂ on ZnO(11 $\bar{2}$ 0) likely proceeds via the formation of the *HOCO intermediate since *HOCO formation ($\Delta E = -0.16$ eV and $E_a = 0.15$ eV) is kinetically more favorable than *HCOO formation ($\Delta E = -1.42$ eV and $E_a = 0.32$ eV). The *HOCO dissociation produces a key reaction intermediate, *CO, along the RWGS + CO-Hydro pathway for CH₃OH synthesis^{27,44}. However, in consideration of the entropic contribution, *CO may not be stable on the ZnO(11 $\bar{2}$ 0) surface under reaction conditions with a BE of –1.33 eV, preferring desorption rather than its further hydrogenation. Thus, CO is predicted to be the product of CO₂ hydrogenation on ZnO(11 $\bar{2}$ 0), which agrees well with the corresponding experimental observation of CO but not CH₃OH as a product of CO₂ hydrogenation on ZnO(11 $\bar{2}$ 0) (see Supplementary Figs. 18, 19).

The DFT optimized geometries at the ZrO₂/ZnO interface were then used to calculate the reaction energy (ΔE) and activation energy (E_a) of each elementary step involved in CO₂ hydrogenation to CH₃OH via the formate pathway, which was identified as an active intermediate by in situ DRIFTS for the CZZ catalysts.

Figure 5b shows the energy profile for the formation of CH₃OH from CO₂ and H₂ along the formate pathway. The initial step in CO₂ hydrogenation, i.e., the formation of the *HCOO intermediate is exothermic with ΔE of –0.52 eV and E_a of 0.78 eV. Further hydrogenations of *HCOO leads to the formations of *H₂COO ($\Delta E = -1.27$ eV; $E_a = 0.66$ eV) and *H₂COOH ($\Delta E = 0.37$ eV; $E_a = 0.52$ eV). Compared with *HCOO hydrogenation to *H₂COO, the *H assisted dissociation to HCO (*HCOO + *H → *HCO + *OH, $\Delta E = -0.44$ eV; $E_a = 1.45$ eV) and subsequently to *CO (*HCO + * → *CO + *H, $\Delta E = 1.51$ eV; $E_a = 1.63$ eV) is kinetically more difficult at the ZnO/ZrO₂ interface. Thus, it suggests that the formation of *CO from *HCOO is highly unlikely, in agreement with the experimental results (Supplementary Figs. 5 and 9). The ZnO–ZrO₂ interface facilitates not only the activation of *HCOO, the rate-limiting step for CO₂ hydrogenation at the ZnO–Cu interface³ via lowering the barrier from 0.85 to 0.66 eV, but also the formation of *H₂COOH, a highly activated step via lowering the barrier from 0.90 to 0.52 → eV. This agrees well with the in situ DRIFTS results (Supplementary Fig. 5), showing a fast conversion of *HCOO to *H₂CO over the CZZ catalyst. *H₂COOH is the precursor for C–O bond breaking as in the case of Cu/ZnO, however, the corresponding barrier ($\Delta E = -1.37$ eV; $E_a = 0.03$ eV) is much lower on ZnO–ZrO₂ than on Cu/ZnO ($E_a = 0.49$ eV)³. The hydrogenation of dissociated *H₂CO results in the formation of *H₃CO ($\Delta E = -0.68$ eV; $E_a = 0.67$ eV) and eventually the production of *CH₃OH ($\Delta E = 0.59$ eV; $E_a = 0.67$ eV). Similar promotion is also observed when compared to Cu/ZrO₂, which shows more difficult activations of *HCOO to *HCOOH

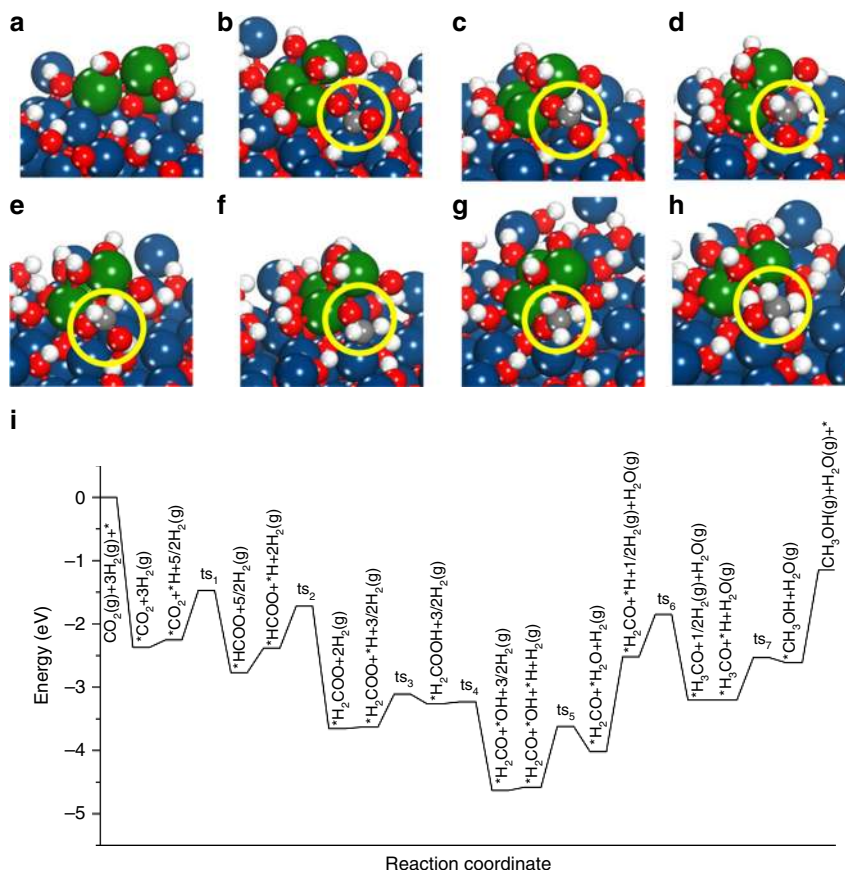


Fig. 5 Density functional theory results. **a–h** DFT optimized configurations of **a** $\text{ZrO}_2/\text{ZnO}(11\bar{2}0)$ and **b** $^*\text{CO}_2$, **c** $^*\text{HCOO}$, **d** $^*\text{H}_2\text{COO}$, **e** $^*\text{H}_2\text{COOH}$, **f** $^*\text{H}_2\text{CO}$, **g** $^*\text{H}_3\text{CO}$, and **h** $^*\text{CH}_3\text{OH}$ adsorbed at the $\text{ZrO}_2/\text{ZnO}(11\bar{2}0)$ interface. $^*(\text{X})$ indicates adsorbed species. The reaction intermediates are shown inside the yellow circle. Dark blue: Zn, green: Zr, red: O, gray: C and white: H. **i** Energy profile for CO_2 hydrogenation to CH_3OH at the $\text{ZrO}_2/\text{ZnO}(11\bar{2}0)$ interface via the formate pathway. “ts” corresponds to the transition state

($\Delta E = 0.70$ eV, $E_a = 0.80$ eV) and $^*\text{H}_2\text{COOH}$ dissociation to $^*\text{H}_2\text{CO}$ and $^*\text{OH}$ ($\Delta E = 0.67$ eV, $E_a = 1.32$ eV) than ZnO-ZrO_2 ²⁷.

For the reaction pathway at the ZnO-ZrO_2 interface, the dissociated $^*\text{OH}$ is removed from the surface by the formation of H_2O , which is an endothermic process ($\Delta E = 0.56$ eV) and has to overcome the highest barrier of 0.96 eV along the pathway. In contrast, it is a facile step at the ZnO-Cu interface ($\Delta E = -0.43$ eV; $E_a = 0.22$ eV)³. Therefore, the potential synergy between the interfaces of ZnO-ZrO_2 and ZnO-Cu might also play an important role in promoting the removal of surface $^*\text{OH}$ to regenerate the active sites. According to the DFT calculated energy barriers, the formation of ZnO-ZrO_2 interface is able to promote the $^*\text{HCOO}$ activations, which have been identified to control the reaction rates at the Cu/ZnO and Cu/ZrO_2 interfaces during CO_2 hydrogenation; yet the removal of $^*\text{OH}$ from the surface to produce gas phase H_2O can be problematic at lower temperatures. Nevertheless, the barrier is <1 eV and is expected to be partially overcome at $T = 493$ K to maintain sufficient amount of active sites for hydrogenation of CO_2 to CH_3OH .

The Cu component was not specifically considered in the present DFT calculations. At the ZnO-ZrO_2 interface, the H_2 dissociative adsorption is an endothermic process ($\Delta E = 0.47$ eV), which is less favorable than that at the $-\text{Cu}/\text{oxide}$ interface ($\Delta E = -0.33$ eV)³. On $\text{Cu}(111)$, H_2 dissociation is thermodynamically and kinetically ($\Delta E = -0.39$ eV; $E_a = 0.53$ eV) more favorable than that on the ZnO-ZrO_2 and Cu/oxide interfaces. Therefore, the presence of Cu is necessary to allow the facile formation of $^*\text{H}$ at the Cu/oxide interface under reaction conditions, which

facilitates the subsequent hydrogenation processes by providing the surface $^*\text{H}$ species. This is consistent with the high pressure in situ DRIFTS (see Fig. 2 and Supplementary Fig. 12) results that CH_3OH is detected over the CZZ sample but not over the ZnO-ZrO_2 sample.

Discussion

For the Cu/ZnO system, the Cu-ZnO interface or the Cu-Zn surface alloy are considered as the active sites for CO_2 hydrogenation to methanol^{3,5–7,24,28,29}. In the case of Cu/ZrO_2 , the Cu-ZrO_2 interface play a very important role for methanol formation^{10,26,27,33}. In both the binary catalysts, the catalytic activity is determined by the Cu-ZnO or Cu-ZrO_2 interaction that is closely related to the physicochemical features (e.g., Cu particle size and surface area of Cu) of Cu species. As shown in the comparison of the catalytic activity of Cu/ZnO , Cu-ZrO_2 , and Cu-ZnO-ZrO_2 in Supplementary Fig. 13, the Cu-ZnO-ZrO_2 ternary catalyst exhibits much higher methanol yield than either Cu-ZnO or Cu-ZrO_2 even though it shows a lower surface area of Cu (S_{Cu}) than the Cu/ZnO catalyst, suggesting that the ZnO-ZrO_2 interaction should also play an important role in the Cu-ZnO-ZrO_2 catalyst for CO_2 hydrogenation. Combining the results of XPS (Supplementary Fig. 17) and CO_2 -TPD (Fig. 4d), it can be concluded that the ZnO-ZrO_2 interaction promotes the formation of oxygen vacancies, which should be the active sites for CO_2 adsorption. The in situ DRIFTS (Fig. 3 and Supplementary Fig. 12) experiments reveal that the

ZnO–ZrO₂ interface is crucial for the transformation of carbonate to formate during CO₂ hydrogenation. However, no surface methoxy, which is a crucial intermediate species for methanol synthesis, is detected on the ZnO–ZrO₂ catalyst (see Fig. 4a–c), while it is abundant on the Cu–ZnO–ZrO₂ catalysts (see Supplementary Figs. 5 and 9). These results indicate that the presence of Cu is necessary for the formate hydrogenation to methoxy in methanol synthesis from CO₂ + H₂. It is reasonable to propose that, in the Cu–ZnO–ZrO₂ system, the ZnO–ZrO₂ interaction contributes to the adsorption of CO₂ and binds the formate intermediate, and the interaction of Cu with the ZnO–ZrO₂ support is responsible for the dissociative adsorption of hydrogen and the subsequent hydrogenation of carbonaceous intermediate species (e.g., formate and methoxy) to methanol. Supplementary Fig. 27 shows an illustration to emphasize on the role of Cu, ZnO, and ZrO₂ in the ternary interaction and a full discussion is also provided.

Both the in situ DRIFTS experiments (Figs. 3 and 4) and DFT calculations (Fig. 5) suggest that CO₂ adsorption and conversion to surface species (e.g., formate) and methanol strongly rely on the ZnO/ZrO₂ interaction, which promotes the *HCOO activations, the rate-limiting step at the Cu/ZnO interface. Such promoting effect can be further enhanced by reducing the particle size of ZnO (Fig. 2 and Supplementary Fig. 8). The DFT results suggest that the presence of Cu at the ZnO–ZrO₂ interface is necessary to provide *H and allows the conversion of the carbonate species to formate, methoxy and eventually methanol, as observed by in situ DRIFT under the activity test condition (Fig. 2) or during the switching from CO₂ to H₂ (Supplementary Fig. 5). Overall, the combination of in situ characterization and DFT calculations enables the identification of active sites and reaction intermediates for the CZZ catalyst during CO₂ hydrogenation and highlights the importance of the strong interplay among Cu, ZnO, and ZrO₂ in promoting the CO₂ conversion and methanol selectivity.

In summary, by designing different Cu–ZnO–ZrO₂ (CZZ) catalysts and performing in situ experiments and DFT calculations, we identified the different functions of the ZnO–ZrO₂ interface and Cu species in the catalytic CO₂ hydrogenation to methanol. The obtained catalysts show very high activity (18.2% of conversion and 80.2% of selectivity obtained at 493 K and 3.0 MPa) for methanol generation. The formate pathway is identified for the CO₂ hydrogenation process over the CZZ catalysts. ZnO–ZrO₂ binary oxides show much higher ability for CO₂ adsorption and the hydrogenation of carbonate species to reactive intermediates (formate and methoxy) than the Cu–ZnO or Cu–ZrO₂ systems. DFT calculations show that the ZnO/ZrO₂ interface is the active site for CO₂ adsorption and conversion, in particular for *HCOO activation, which is the rate-limiting step at the Cu/ZnO interface during CO₂ hydrogenation. The presence of Cu⁰ is also necessary to allow the formation of *H under reaction conditions, while tuning the interaction between ZnO and ZrO₂ can affect the formation and evolution of the surface species, therefore controlling the catalytic performance. The findings proposed in this work would enrich the knowledge in understanding the fundamental features of the CZZ ternary CO₂ hydrogenation catalysts and be helpful for designing complex catalysts with multiple active components.

Methods

3DOM catalyst preparation. 3DOM catalysts were prepared by a colloidal crystal template method. First, uniform monodisperse poly methyl methacrylate (PMMA) spheres were synthesized as template via an emulsifier-free emulsion polymerization route⁴⁵. After that, the required amounts of Cu(NO₃)₂·3H₂O, Zn(NO₃)₂·6H₂O, and Zr(NO₃)₄·5H₂O were dissolved in 20 mL of deionized water to form a

transparent solution (5 mol/L, Cu/Zn/Zr molar ratio = 5:2:3), and then 10 g of citric acid (C₆H₈O₇·H₂O) was added into the solution and dissolved at 333 K under stirring for 1 h. Then, 10 mL of ethylene glycol (EG) was added into the solution under stirring for 10 min. Subsequently, the dried PMMA templates were soaked in the precursor solutions for 6 h. After being filtered, the precursors were dried at 333 K for 12 h. Finally, the precursors were calcined at 723 K for 6 h with a ramp rate of 1, 2, 4, and 8 K/min under air, respectively. The obtained samples were labeled as M-CZZ(16), M-CZZ(19), M-CZZ(24), and M-CZZ(36).

Cu–ZnO (molar ratio of Cu/Zn = 5:2), Cu–ZrO₂ (molar ratio of Cu/Zr = 7:3), and ZnO–ZrO₂ (molar ratio of Zn/Zr = 7:3) samples were prepared by a co-precipitation method. The required amounts of Cu(NO₃)₂·3H₂O, Zn(NO₃)₂·6H₂O, and/or Zr(NO₃)₄·5H₂O were dissolved in 20 mL of deionized water to form a transparent solution (5 mol/L). Then, the transparent solution and NH₃·H₂O (2.5 wt.%) was added dropwise into 200 mL of deionized water, simultaneously, controlling the pH at ~6.5. After aging for 1 h, the precursor was filtered and washed with deionized water. The precursors were then dried at 333 K for 12 h and further calcined at 723 K for 3 h with a ramp rate of 2 K/min.

The ZnO–ZrO₂ (molar ratio of Zn/Zr = 7:3) catalysts with different particle size of ZnO were also prepared by a co-precipitation method using different precipitating agent. The catalyst precipitated with sodium carbonate and calcined at 673 K for 6 h with a ramp rate of 1 K/min under air was labeled as ZnO(15)–ZrO₂. The catalyst precipitated with sodium carbonate and calcined at 723 K for 6 h with a ramp rate of 1 K/min under air was labeled as ZnO(21)–ZrO₂. The catalyst precipitated with NH₃·H₂O (2.5 wt.%) and calcined at 723 K for 6 h with a ramp rate of 2 K/min under air was labeled as ZnO(42)–ZrO₂.

Preparation of the nonporous samples. Conventional catalysts were prepared by a co-precipitation method. The required amounts of Cu(NO₃)₂·3H₂O, Zn(NO₃)₂·6H₂O, and Zr(NO₃)₄·5H₂O were dissolved in 20 mL of deionized water to form a transparent solution (5 mol/L, Cu/Zn/Zr molar ratio = 5:2:3). Then, the transparent solution and NH₃·H₂O (2.5 wt.%) was added dropwise into 200 mL of deionized water, simultaneously, controlling the pH at ~6.5. After aging for 1 h, the precursor was filtered and washed with deionized water. The precursors were then dried at 333 K for 12 h and further calcined at 723 K for 3 h with a ramp rate of 2 and 5 K/min, and the obtained samples are labeled as N-CZZ(25) and N-CZZ(31), respectively. When the precipitating agent was changed from sodium carbonate (0.5 mol/L) to NH₃·H₂O (2.5 wt.%) and calcining the precursor at 723 K for 3 h with a ramp rate of 5 K/min, the obtained sample was labeled as N-CZZ(43).

Characterization. The specific surface area of the catalysts was calculated according to the BET method using the N₂ adsorption isotherm at 77 K obtained on a Quantachrome Autosorb-iQ instrument. The crystal phases of the prepared catalysts were identified using a powder X-ray diffractometer (Rigaku D/max-R) with Cu Kα radiation (λ = 0.15406 nm). The X-ray tube was operated at 40 kV and 40 mA. The XRD patterns were recorded for 2θ values ranging from 20° to 80° at a scanning rate of 2°/min. The morphology of the catalysts was observed by the scanning electron microscopy (SEM) and transmission electron microscopy (TEM) technology. The SEM measurement was performed on a Nova NanoSEM 450 instrument using an accelerating voltage of 2000 V–30 kV. The SEM samples were dusted on an adhesive conductive carbon belt attached to a copper disk and coated with 2–3 nm Pt prior to the measurement. For TEM characterization, a Tecnai G² TF30 S-Twin microscope was used operating at 300 kV. The specimens were crushed into powder and immersed in a small volume of ethanol. After sonicating the mixture for 10 min, a droplet of the suspension was allowed to dry on a holey carbon/Formvar-coated copper TEM grid.

XPS dates were obtained with a PHI 5000 Versaprobe II system equipped with a monochromatic Al-Kα X-ray source. The reduced samples were placed on stainless steel sample-holders were transferred to the XPS pre-chamber under inert atmosphere and stayed there for 12 h in a vacuum atmosphere. The spectra were recorded after purging the samples at ambient temperature under vacuum (residual pressure < 10^{−7} Pa). The C 1s signal at 284.8 eV was used as an internal standard for calibration of the XPS signals.

H₂ temperature-programmed reduction (H₂-TPR) was performed on a ChemBET Pulsar & TPR/TPD apparatus (Quantachrome Instruments) with a thermal conductivity detector (TCD). Prior to each experiment, the sample (50 mg) was pre-treated in flowing pure He (30 mL/min) at 573 K for 1 h and cooled to room temperature (RT). Thereafter, the temperature was increased at a rate of 10 K/min to 673 K in flowing 10% H₂/Ar (30 mL/min). The metallic copper surface area (S_{Cu}) was measured using N₂O decomposition method. The catalyst (50 mg) was first reduced with 10% H₂/Ar (30 mL/min) at 573 K for 1 h followed by purging with He (30 mL/min) for 30 min and cooling to 333 K. Then, a flow of 10% N₂O/He (30 mL/min) gas was fed into the reactor for 1 h. TPR measurement was subsequently performed under a 10% H₂/Ar flow (30 mL/min) to 573 K with a ramp rate of 10 K/min. The copper surface area was calculated on base of Eq. (1) by assuming that the copper crystallites are spherical.

$$S_{Cu} (m^2/g_{cat}) = [200(\text{Mol } H_2) \times (SF) \times (N_A)] / (SD_{Cu}) \quad (1)$$

$$D_{Cu} (%) = [\text{the amount of exposed copper}] / [\text{the total amount of copper atoms}] \quad (2)$$

Where M_{H_2} is the amount of H_2 consumed during the TPR step per unit mass of the catalyst ($\text{mol H}_2/\text{g}_{\text{cat}}$), SF is the stoichiometric factor (2.0), N_A is Avogadro's number (6.022×10^{23} atoms/mol) and SD_{Cu} is the copper surface density (1.47×10^{19} atoms/ m^2).

$$\text{TOF}_{\text{Cu}} = \frac{P_{\text{CH}_3\text{OH}} \times M_{\text{Cu}}}{3600 \times 1000 \times (D \times 0.01) \times X_{\text{Cu}}} \quad (3)$$

Where $P_{\text{CH}_3\text{OH}}$, M_{Cu} , D , X_{Cu} are CH_3OH productivity (expressed in $\text{mol h}^{-1} \text{kg}^{-1}$), the copper molecular weight, the copper dispersion (expressed in %), the average mass fraction of Cu in fresh catalyst, respectively.

CO temperature-programmed reduction (CO -TPR) was performed on a the CATLAB catalyst characterization system (Hiden Analytical Co., England). Prior to each experiment, the sample (50 mg) was pre-treated in flowing pure He (30 mL/min) at 573 K for 1 h and then cooled to RT. Thereafter, the temperature was increased at a rate of 10 K/min to 973 K in flowing 10% CO/Ar (30 mL/min). The gas was analyzed by an online mass spectrometer (MS).

CO_2 temperature-programmed desorption (CO_2 -TPD) was performed on a ChemBET Pulsar & TPR/TPD apparatus (Quantachrome Instruments) equipped with a TCD. Prior to each experiment, the sample (50 mg) was pre-treated in flowing pure He (30 mL/min) at 573 K for 1 h and then cooled to RT. Thereafter, the temperature was increased at a rate of 10 K/min to 573 K in flowing 10% H_2/Ar (30 mL/min) and holding at 573 K for 30 min. Thereafter, the pre-treated sample was exposed to CO_2 (30 mL/min) and He (30 mL/min) at RT for 30 min, respectively. After that, the temperature was increased at a rate of 10 K/min to 873 K in flowing He (30 mL/min).

In situ DRIFTS measurements were performed on an FTIR spectrometer (vertex 70, Bruker, Germany) equipped with a liquid nitrogen N_2 cooled mercury–cadmium–telluride (MCT) detector. The scans were collected from 4000 to 600 cm^{-1} at a resolution of 4 cm^{-1} . The catalyst powders were placed in a high-pressure (0–10 MPa) DRIFTS cell (HC-900, Pike Technologies) equipped with ZnSe windows. To remove the possible residual surface species prior to testing, each sample was heated at 573 K for 2 h in a 40 mL/min flow of He. Then, the sample was cooled to 323 K and switching feed to 10% H_2/He mixture at a flow rate of 40 mL/min while increasing the temperature to 573 K for 1 h. After that, the sample was flushed with He (40 mL/min) for 1 h and cooled to 493 K prior to sample testing. The background subtractions were executed over different samples for testing in a 40 mL/min He under different reaction condition (atmospheric pressure or 3 MPa). After that, the reaction gases were switched into the reaction chamber, the evolutions of functional groups on samples surfaces were recorded by FTIR spectrometer.

Activity test. The activity test for CO_2 hydrogenation to methanol were performed in a high-pressure fixed-bed flow stainless steel reactor. One gram of catalyst was diluted with quartz sand (both in 20–40 mesh), and then packed into the stainless steel tubular reactor. Prior to the catalytic measurements, the catalyst was reduced in a stream of 10% H_2/N_2 at 573 K for 6 h under atmospheric pressure. Then, the temperature was cooled to 323 K, and the reductive gas was replaced by the reaction gas (24.4% CO_2 and 75.6% H_2). The reaction was performed with a pressure of 3.0 MPa, reaction gases flow rate is 100 mL/min, and the temperature at 493 K. Each reaction was conducted under these conditions for 16 h. The reactants and products flowing out in the reactors were passed through the gas/liquid separator connected to a heat exchanger (273 K) and then analyzed by an online gas chromatographer (GC, Agilent Technologies 6890A) equipped with a TCD and a flame ionization detector (FID). The CO_2 conversion and CH_3OH selectivity were obtained from the GC data.

Computational methods. Spin polarized density functional theory (DFT)^{46,47} calculations were performed using the Vienna Ab-Initio Simulation Package (VASP) code.^{48,49} Projector augmented wave (PAW)⁵⁰ potentials were used to describe the core electrons with the generalized gradient approximation (GGA) using PW91 functionals⁵¹. The Kohn–Sham one-electron wave functions were expanded by using a plane wave basis set with a kinetic energy cutoff of 400 eV.

The lattice parameters of bulk ZnO was calculated using a $12 \times 12 \times 8$ Monkhorst⁵² pack meshes. Our calculated lattice parameters of $a = b = 3.194 \text{ \AA}$ and $c/a = 1.608 \text{ \AA}$ are similar to the previously calculated values of $a = b = 3.159 \text{ \AA}$ and $c/a = 1.608$ using DFT⁵³. The ZnO(110) surface was modeled using a six layer 3×3 surface slab. The ZrO_2/ZnO interface was modeled by depositing a small ZrO_2 cluster on ZnO(110) surface. Surface O atoms on ZrO_2 cluster and ZnO(110) surface were hydroxylated to take into account of the H-spillover under the H_2 -rich conditions used for CO_2 hydrogenation. The electronic structure of Zn in ZnO was treated in the DFT + U ⁵⁴ formalism with a U value of 7.5 eV⁵³. The Brillouin zone of the ZnO(110) surface was sampled using the Γ -point. A 18 Å thick vacuum was added along the direction perpendicular to the surface in the initial slab model to avoid the artificial interactions between the slab and its periodic images. During geometry optimization, the atoms in the bottom three layers were fixed while all other atoms were allowed to relax until Hellman–Feynman force on each ion was smaller than 0.02 eV/ Å . The binding energy (BE) of an adsorbate was calculated as follows:

$$\text{BE} = E(\text{slab} + \text{adsorbate}) - E(\text{slab}) - E(\text{adsorbate})$$

where $E(\text{slab} + \text{adsorbate})$, $E(\text{slab})$, and $E(\text{adsorbate})$ are the total energies of the slab with adsorbate, clean slab, and adsorbate species in the gas phase, respectively.

The transition state of a chemical reaction was located using the climbing image nudged elastic band (CI-NEB) method implemented in VASP⁵⁵. The activation energy (E_a) of a chemical reaction is defined as the energy difference between the initial and transition states while the reaction energy (ΔE) is defined as the energy difference between the initial and final states.

Data availability

All data are available from the authors on reasonable request.

Received: 6 November 2018 Accepted: 14 February 2019

Published online: 11 March 2019

References

- Álvarez, A. et al. Challenges in the greener production of formates/formic acid, methanol, and DME by heterogeneously catalyzed CO_2 hydrogenation processes. *Chem. Rev.* **117**, 9804 (2017).
- Graciani, J. et al. Highly active copper-ceria and copper-ceria-titania catalysts for methanol synthesis from CO_2 . *Science* **345**, 546–550 (2014).
- Kattel, S., Ramírez, P. J., Chen, J. G., Rodríguez, J. A. & Liu, P. Active sites for CO_2 hydrogenation to methanol on Cu/ZnO catalysts. *Science* **357**, 1296–1299 (2017).
- Bernskoetter, W. H. & Hazari, N. Reversible hydrogenation of carbon dioxide to formic acid and methanol: Lewis acid enhancement of base metal catalysts. *Acc. Chem. Res.* **50**, 1049–1058 (2017).
- Kattel, S., Liu, P. & Chen, J. G. Tuning selectivity of CO_2 hydrogenation reactions at the metal/oxide interface. *J. Am. Chem. Soc.* **139**, 9739 (2017).
- Berg, R. V. D. et al. Structure sensitivity of Cu and CuZn catalysts relevant to industrial methanol synthesis. *Nat. Commun.* **7**, 13057 (2016).
- Behrens, M. et al. The active site of methanol synthesis over Cu/ZnO/ Al_2O_3 industrial catalysts. *Science* **336**, 893 (2012).
- Arena, F. et al. Synthesis, characterization and activity pattern of Cu–ZnO/ZrO₂ catalysts in the hydrogenation of carbon dioxide to methanol. *J. Catal.* **249**, 185–194 (2007).
- Guo, X., Mao, D., Lu, G., Wang, S. & Wu, G. Glycine-nitrate combustion synthesis of CuO–ZnO–ZrO₂ catalysts for methanol synthesis from CO_2 hydrogenation. *J. Catal.* **271**, 178–185 (2010).
- Arena, F. et al. Solid-state interactions, adsorption sites and functionality of Cu–ZnO/ZrO₂ catalysts in the CO_2 hydrogenation to CH_3OH . *Appl. Catal. A* **350**, 16–23 (2008).
- Gao, P. et al. Influence of Zr on the performance of Cu/Zn/Al/Zr catalysts via hydrothermal-like precursors for CO_2 hydrogenation to methanol. *J. Catal.* **298**, 51–60 (2013).
- Bonura, G., Cordaro, M., Cannilla, C., Arena, F. & Frusteri, F. The changing nature of the active site of Cu–Zn–Zr catalysts for the CO_2 hydrogenation reaction to methanol. *Appl. Catal. B* **152–153**, 152–161 (2014).
- Phongamwong, T. et al. CO_2 hydrogenation to methanol over CuO–ZnO–ZrO₂–SiO₂ catalysts: Effects of SiO₂ contents. *Chem. Eng. J.* **316**, 692–703 (2017).
- Witoon, T. et al. Tuning of catalytic CO_2 hydrogenation by changing composition of CuO–ZnO–ZrO₂ catalysts. *Energ. Convers. & Manag.* **118**, 21–31 (2016).
- Frei, E., Schaadt, A., Ludwig, T., Hillebrecht, H. & Krossing, I. The influence of the precipitation/ageing temperature on a Cu/ZnO/ZrO₂ catalyst for methanol synthesis from H_2 and CO_2 . *Chemcatchem* **6**, 1721–1730 (2014).
- Li, L., Mao, D., Yu, J. & Guo, X. Highly selective hydrogenation of CO_2 to methanol over CuO–ZnO–ZrO₂ catalysts prepared by a surfactant-assisted co-precipitation method. *J. Power Sources* **279**, 394–404 (2015).
- Dong, X. et al. CO_2 hydrogenation to methanol over Cu/ZnO/ZrO₂ catalysts prepared by precipitation-reduction method. *Appl. Catal. B* **191**, 8–17 (2016).
- Wang, W., Wang, S., Ma, X. & Gong, J. Recent advances in catalytic hydrogenation of carbon dioxide. *Chem. Soc. Rev.* **40**, 3703 (2011).
- Kuld, S. et al. Quantifying the promotion of Cu catalysts by ZnO for methanol synthesis. *Science* **352**, 969 (2016).
- Arena, F. et al. Effects of oxide carriers on surface functionality and process performance of the Cu–ZnO system in the synthesis of methanol via CO_2 hydrogenation. *J. Catal.* **300**, 141–151 (2013).
- Grunwaldt, J. D., Molenbroek, A. M., Topsøe, N. Y., Topsøe, H. & Clausen, B. S. In Situ Investigations of Structural Changes in Cu/ZnO Catalysts. *J. Catal.* **194**, 452–460 (2000).
- Valant, A. L. et al. The Cu–ZnO synergy in methanol synthesis from CO_2 , Part 1: origin of active site explained by experimental studies and a sphere

- contact quantification model on Cu+ZnO mechanical mixtures. *J. Catal.* **324**, 41–49 (2015).
23. Bu, L. et al. Biaxially strained PtPb/Pt core/shell nanoplate boosts oxygen reduction catalysis. *Science* **354**, 1410 (2016).
24. Vesborg, P. C. K. et al. Transient behavior of Cu/ZnO-based methanol synthesis catalysts. *J. Catal.* **262**, 65–72 (2009).
25. Meunier, F. C. Mixing copper nanoparticles and ZnO nanocrystals: a route towards understanding the hydrogenation of CO₂ to methanol? *Angew. Chem. Int. Ed.* **50**, 4053–4054 (2011).
26. Ro, I. et al. The role of the Cu-ZrO₂ interfacial sites for ethanol conversion to ethyl acetate and methanol synthesis from CO₂ and H₂. *ACS Catal.* **6**, 7040–7050 (2016).
27. Kattel, S., Yan, B. H., Yang, Y. X., Chen, J. G. G. & Liu, P. Optimizing binding energies of key intermediates for CO₂ hydrogenation to methanol over oxide-supported copper. *J. Am. Chem. Soc.* **138**, 12440–12450 (2016).
28. Lunkenbein, T., Schumann, J., Behrens, M. & Willinger, M. G. Formation of a ZnO overlayer in industrial Cu/ZnO/Al₂O₃ catalysts induced by strong metal-support interaction. *Angew. Chem. Int. Ed.* **54**, 4544–4548 (2015).
29. Liao, F. et al. Electronic modulation of a copper/zinc oxide catalyst by a heterojunction for selective hydrogenation of carbon dioxide to methanol. *Angew. Chem. Int. Ed.* **51**, 5832–5836 (2012).
30. Liao, F. et al. Morphology-dependent interactions of ZnO with Cu nanoparticles at the materials' interface in selective hydrogenation of CO₂ to CH₃OH. *Angew. Chem. Int. Ed.* **123**, 2210–2213 (2015).
31. Galván, C. Á. et al. Reverse water-gas shift reaction at the Cu/ZnO interface: influence of the Cu/Zn ratio on structure-activity correlations. *Appl. Catal. B* **195**, 104–111 (2016).
32. Wang, Y. H. et al. Structure-activity relationships of Cu-ZrO₂ catalysts for CO₂ hydrogenation to methanol: interaction effects and reaction mechanism. *RSC Adv.* **7**, 8709–8717 (2017).
33. Fisher, I. A., Bell, A. T., Fisher, I. A. & Bell, A. T. In situ infrared study of methanol synthesis from H₂/CO over Cu/SiO₂ and Cu/ZrO₂/SiO₂. *J. Catal.* **172**, 222–237 (1998).
34. Wang, J. et al. A highly selective and stable ZnO-ZrO₂ solid solution catalyst for CO₂ hydrogenation to methanol. *Sci. Adv.* **3**, e1701290 (2017).
35. Yang, R., Zhang, Y., Iwama, Y. & Tsubaki, N. Mechanistic study of a new low-temperature methanol synthesis on Cu/MgO catalysts. *Appl. Catal. A* **288**, 126–133 (2005).
36. Qi, S., Liu, C. W., Wei, P., Zhu, Q. M. & Deng, J. F. In situ IR studies on the mechanism of methanol synthesis over an ultrafine Cu/ZnO/Al₂O₃ catalyst. *Appl. Catal. A* **171**, 301–308 (1998).
37. Sato, A. G. et al. Effect of the ZrO₂ phase on the structure and behavior of supported Cu catalysts for ethanol conversion. *J. Catal.* **307**, 1–17 (2013).
38. Du, H., Williams, C. T., Ebner, A. D. & Ritter, J. A. In situ FTIR spectroscopic analysis of carbonate transformations during adsorption and desorption of CO₂ in K-promoted HTlc. *Chem. Mater.* **22**, 3519–3526 (2010).
39. Kurtz, M. et al. Active sites on oxide surfaces: ZnO-catalyzed synthesis of methanol from CO and H₂. *Angew. Chem. Int. Ed.* **44**, 2790–2794 (2005).
40. Rhodes, M. D. & Bell, A. T. The effects of zirconia morphology on methanol synthesis from CO and H₂ over Cu/ZrO₂ catalysts: Part I. Steady-state studies. *J. Catal.* **233**, 198–209 (2005).
41. Rhodes, M. D., Pokrovski, K. A. & Bell, A. T. The effects of zirconia morphology on methanol synthesis from CO and H₂ over Cu/ZrO₂ catalysts: Part II. Transient-response infrared studies. *J. Catal.* **233**, 210–220 (2005).
42. Kurtz, M. et al. Active sites on oxide surfaces: ZnO-catalyzed synthesis of methanol from CO and H₂. *Angew. Chem. Int. Ed.* **44**, 2790–2794 (2005).
43. French, S. A. et al. From CO₂ to methanol by hybrid QM/MM embedding. *Angew. Chem. Int. Ed.* **40**, 4437–4440 (2001).
44. Yang, Y. X., White, M. G. & Liu, P. Theoretical study of methanol synthesis from CO₂ hydrogenation on metal-doped Cu(111) surfaces. *J. Phys. Chem. C* **116**, 248–256 (2012).
45. Xie, S. H. et al. Au/3DOM Co₃O₄: highly active nanocatalysts for the oxidation of carbon monoxide and toluene. *Nanoscale* **5**, 11207–11219 (2013).
46. Hohenberg, P. & Kohn, W. Inhomogeneous electron gas. *Phys. Rev. B* **136**, B864–B871 (1964).
47. Kohn, W. & Sham, L. J. Self-consistent equations including exchange and correlation effects. *Phys. Rev.* **140**, A1133–A1138 (1965).
48. Kresse, G. & Furthmüller, J. Efficiency of ab-initio total energy calculations for metals and semiconductors using a plane-wave basis set. *Comp. Mater. Sci.* **6**, 15–50 (1996).
49. Kresse, G. & Furthmüller, J. Efficient iterative schemes for ab initio total-energy calculations using a plane-wave basis set. *Phys. Rev. B* **54**, 11169–11186 (1996).
50. Blochl, P. E. Projector augmented-wave method. *Phys. Rev. B* **50**, 17953–17979 (1994).
51. Perdew, J. P. & Wang, Y. Accurate and simple analytic representation of the electron-gas correlation-energy. *Phys. Rev. B* **45**, 13244–13249 (1992).
52. Monkhorst, H. J. & Pack, J. D. Special points for Brillouin-zone integrations. *Phys. Rev. B* **13**, 5188–5192 (1976).
53. Tang, Q. L. & Luo, Q. H. Adsorption of CO₂ at ZnO: a surface structure effect from DFT+U calculations. *J. Phys. Chem. C* **117**, 22954–22966 (2013).
54. Dudarev, S. L., Botton, G. A., Savrasov, S. Y., Humphreys, C. J. & Sutton, A. P. Electron-energy-loss spectra and the structural stability of nickel oxide: an LSDA+U study. *Phys. Rev. B* **57**, 1505–1509 (1998).
55. Henkelman, G., Uberuaga, B. P. & Jonsson, H. A climbing image nudged elastic band method for finding saddle points and minimum energy paths. *J. Chem. Phys.* **113**, 9901–9904 (2000).

Acknowledgements

We thank Xiaodong Wang, Jian Lin, and Chuande Huang for helpful discussions. This work was partly supported by the National Natural Science Foundation of China (Nos. 51774159, 51304099, and 51404122), the National Key Technologies R & D Program of China (2011BAC01B03), the Candidate Talents Training Fund of Yunnan Province (Nos. 2014HB006), and the Qinglan Project of Kunming University of Science and Technology. Work performed at Brookhaven National Laboratory (BNL) was sponsored by the United States Department of Energy (U.S. DOE), Office of Science, under Contract No. DE-SC0012704. We also thank the Center for Functional Nanomaterials, a user facility at BNL that is supported by the U.S. DOE Office under Contract No. DE-AC02-05CH11231.

Author contributions

Y.W. and W.G. performed the catalyst preparation, catalytic tests, and high-pressure in situ DRIFTS measurement. K.L. designed the catalysts and contributed to the characterizations. S.K. and P.L. conducted the DFT calculations and wrote part of the paper (calculation). H.W., J.G.C., and K.L. designed the study, analyzed the data, and co-wrote the paper. All the authors discussed the results.

Additional information

Supplementary Information accompanies this paper at <https://doi.org/10.1038/s41467-019-09072-6>.

Competing interests: The authors declare no competing interests.

Reprints and permission information is available online at <http://npg.nature.com/reprintsandpermissions/>

Journal peer review information: *Nature Communications* thanks Xinwen Guo, and other anonymous reviewer(s) for their contribution to the peer review of this work. Peer reviewer reports are available.

Publisher's note: Springer Nature remains neutral with regard to jurisdictional claims in published maps and institutional affiliations.



Open Access This article is licensed under a Creative Commons Attribution 4.0 International License, which permits use, sharing, adaptation, distribution and reproduction in any medium or format, as long as you give appropriate credit to the original author(s) and the source, provide a link to the Creative Commons license, and indicate if changes were made. The images or other third party material in this article are included in the article's Creative Commons license, unless indicated otherwise in a credit line to the material. If material is not included in the article's Creative Commons license and your intended use is not permitted by statutory regulation or exceeds the permitted use, you will need to obtain permission directly from the copyright holder. To view a copy of this license, visit <http://creativecommons.org/licenses/by/4.0/>.

© The Author(s) 2019